ADVANCED FUNCTIONAL MATERIALS
www.afm-journal.de

Exploring Dipolar Dynamics and Ionic Transport in Metal-Organic Frameworks: Experimental and Theoretical Insights

*Ralph Freund, Arthur Schulz, Peter Lunkenheimer, Maryana Kraft, Thomas Bergler, Harald Oberhofer, and Dirk Volkmer**

The present study examines the potential coupling between dipolar dynamics and ionic charge transport in metal-organic framework (MOF) compounds. MOFs are known for their high porosity and customizable properties. By integrating freely rotating dipolar groups into the ligands, a novel structure, CFA-25, akin to the known BUT-2 framework, is synthesized. This facilitated the investigation of local and macroscopic effects, particularly the possible interplay between dipolar units and Cs cations. The research aimed to understand fundamental dipolar dynamics and ionic charge transport, employing Cs ions for their X-ray diffraction characterizability. Experimental analysis using dielectric spectroscopy, complemented by theoretical simulations, explored questions regarding glassy freezing of re-orientational dynamics, Cs cation motion within the network, and the influence of dipolar units on transport. Contrary to previous reports, this work finds that Cs transport exhibits substantial barriers, necessitating specialized simulation techniques for accurate characterization. This interdisciplinary approach sheds light on the intricate dynamics of MOFs and offers insights into their potential applications involving ion transport phenomena.

1. Introduction

Metal-organic framework compounds are characterized not only by extremely high porosity and correspondingly large internal surfaces,[1] but also by an almost limitless scope for design: Properties and topology of the networks can be influenced not merely by the choice of metal centers and the denticity of the ligands,[2] the modification of the latter allows fine-tuning of the physical and chemical characteristics to almost any application.[3] Strictly localized molecular properties such as acidity and basicity, electrical and thermal conductivity, biological activity, and more can also be incorporated into the networks, which can have both local and macroscopic effects.[4] One such possible modification is the integration of dipolar groups into the organic linker. Selecting the design to enable rotational motions of the dipolar group, allows the integration of these molecular dynamics into a crystalline network. On the one hand, these dipoles can interact locally with each other and with charged particles that are not part of the network, contributing, for example, to their transport. On the other hand, macroscopic interactions are also possible.[5] It should be noted that MOFs, featuring dipolar linker groups with rotational degrees of freedom, in some respect resemble plastic crystals. The latter are formed by dipolar molecules whose centers of gravity are located on a crystalline lattice while they are still able to rotate.[6] While these dipolar reorientations in plastic crystals usually are isotropic, the rotation axes of linker-related dipoles in MOFs are fixed. However, at low temperatures the rotational motions in plastic crystals also often become anisotropic.[6] Interestingly, various plastic crystals containing ionic species as Li^+ or Na^+ were found to reveal rather high ionic conductivity.[6,7,8–10] This makes them promising candidates for solid-state electrolytes in energy-storage devices like batteries. It seems that in these materials the dipolar rotations lead to an enhancement of ionic motions via a revolving-door or paddle-wheel like mechanism.[8,11,12] Interestingly, in Ref. [13], a coupling of rotational dynamics of dipolar units and ionic transport was also discussed for a crystalline dielectric material comprising dipolar cations confined in supramolecular cages. Moreover, based on dielectric experiments, the facilitation of ionic charge transport by dipole rotations was also considered for certain ionic liquids and deep eutectic solvents.[14,15] The question arises whether such a mechanism could also be active in MOFs. Dielectric spectroscopy

R. Freund, M. Kraft, D. Volkmer
Chair of Solid State and Materials Chemistry
University of Augsburg, Institute of Physics
Universitaetsstrasse 1, 86159 Augsburg, Germany
E-mail: dirk.volkmer@physik.uni-augsburg.de
A. Schulz, P. Lunkenheimer
Experimental Physics V, Center for Electronic Correlations and Magnetism
University of Augsburg, Institute of Physics
Universitaetsstrasse 1, 86159 Augsburg, Germany
T. Bergler, H. Oberhofer
Department of Physics and Bavarian Center for Battery Technologies
University of Bayreuth
95447 Bayreuth, Germany

The ORCID identification number(s) for the author(s) of this article can be found under https://doi.org/10.1002/adfm.202415376

DOI: 10.1002/adfm.202415376

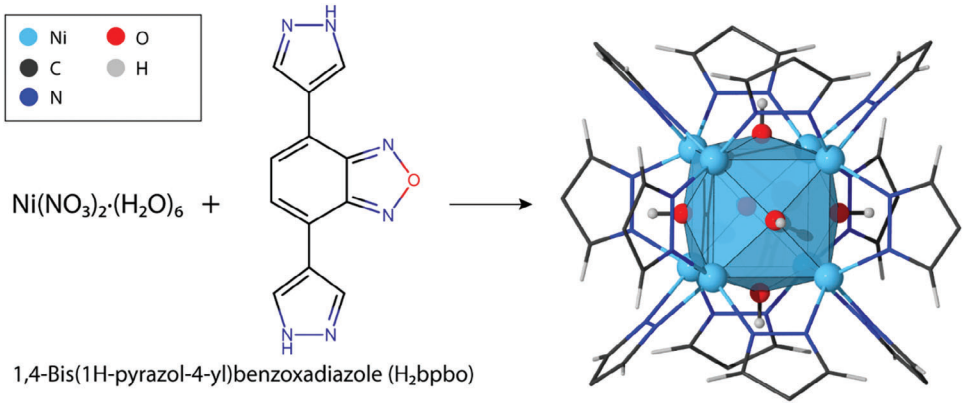

Scheme 1. Synthesis of $(DMA^+)_2[Ni_8(OH)_6(bpbo)_6]$ (CFA-25) through the reaction of Nickel nitrate hexahydrate and 1,4-Bis(1H-pyrazol-4-yl)benzoxadiazole (H_2bpbo) in a mixture of water and dimethylacetamide (DMA). The scheme highlights a single secondary building unit of CFA-25, showing the coordination environment around the Ni_8 cluster, but omits the full unit cell structure for clarity.

as employed in the present work is able to detect both dipolar rotational motions and ionic conductivity and therefore is ideally suited to check for a possible coupling of these dynamics.

In the study presented here, we explore just such effects. For this purpose, a network was synthesized based on the literature known structure BUT-2,[16] however, with freely rotating groups characterized by an extremely large dipole moment integrated into the ligands (**Scheme 1**). The so obtained isotypic structure CFA-25 also exhibits an anionic character, similar to the structure BUT-2.[17] Exploiting this characteristic, in a second step Cs cations were integrated into the network. Thus, a complex network was obtained, allowing the study of local effects, such as the mutual influence of the dipoles, as well as the interactions between the dipoles and Cs cations. We want to point out that here we do not aim at the development of a superionic conductor (for this purpose Li or Na ions would be better suited than the rather large Cs ions). Instead, we intend to investigate dipolar dynamics and ionic charge transport and their possible coupling in a MOF with dipolar linker groups on a fundamental level (which is why Cs ions were chosen, allowing the characterization of the positions by X-ray diffraction). Especially, the macroscopic dynamics of both the dipolar units and the positively charged Cs cations in an electric field were examined to answer the following questions: Is there glassy freezing of the re-orientational dynamics, analogous to plastic crystals? How is the motion of the Cs cations in the network affected? Is the motion positively influenced by the dipoles ("revolving-door" or "paddle wheel" principle as in plastic crystals) or is the transport hindered? How does the transport differ between the different Cs positions?

In answering these questions, we supplement our experimental efforts with some theoretical simulations, both on the level of electronic density functional theory and more approximate classical force fields. These serve to uncover pathways of ion transport and gauge the barriers and bottlenecks of Cs cation transport processes. Contrary to many earlier reports of combined experimental and theoretical studies of ion transport in MOFs,[18] Cs transport here is subject to substantial barriers, making it hard to tackle with unaccelerated dynamical simulations. Instead, as detailed below, we rely on techniques that directly sample ionic probabilities and transition states.

2. Results and Discussion

In total, three different synthesis routes yield $X_{2-x}[Ni_8(OH)_{6-x}(H_2O)_x(bpbo)_6]$ (X = cation$^+$, CFA-25), one for the synthesis of microcrystalline products, two for the synthesis of single crystals. Defined single crystals with dimensions sometimes exceeding 100 µm could be obtained by reacting $Ni(NO_3)_2{\bullet}(H_2O)_6$ and H_2bpbo in a water-DMAc mixture in a Teflon-lined autoclave for several days at 160 °C (Figures S4 and S6, Supporting Information). However, PXRD (Figure S1, Supporting Information) and IR measurements (Figure S3, Supporting Information) indicated synthesis-related impurities of $Ni(OH)_2$. By lowering the water-DMAc ratio, a phase-pure product was achieved, albeit leading to a strong intergrowth of crystals. Nevertheless, isolated single crystals could be detected. A phase-pure microcrystalline product was prepared by reacting $Ni(AcO)_2{\bullet}(H_2O)_4$ and H_2bpbo dissolved in a water-DMAc mixture in a Teflon-lined autoclave overnight at 135 °C.

CFA-25 crystallizes in the cubic space group $Fm\bar{3}m$ (no. 225, see Table S1, Supporting Information). The basic structure of the network is identical to the reference structure $X_{2-x}[Ni_8(OH)_{6-x}(H_2O)_x(bdp)_6]$,[16] except for the additional bipolar unit at the linkers. The nickel cations form a cube-shaped secondary building unit (SBU), with the faces being bridged by hydroxide ions, and the edges being bridged by pyrazolate groups of the organic linker, which simultaneously span the 3D network (**Figure 1a**). The organic linker consists of two terminal pyrazoles bridged by a 2,1,3-benzoxadiazole unit linked with single bonds. The central unit is characterized by a high dipole moment of ≈4.04 D.[19] This dipole moment is reproduced in our classical simulations (≈3.92 D) based on the REPEAT charge model.[20] Due to this and the linkage motif, the detection of rotation within the linker with dielectric spectroscopy is possible, as we will show below. **Figure 2** depicts the torsional potential calculated in vacuum as a function of the rotation angle of the benzoxadiazole unit and the phenyl unit of the reference structure. For the former, torsional potential energy minima are found for angles of about 0° and 180°, allowing a fully planar arrangement of rotor and stator units (cf. Figure 1a). Note that we thereby disregard all possible interactions of the rotors with

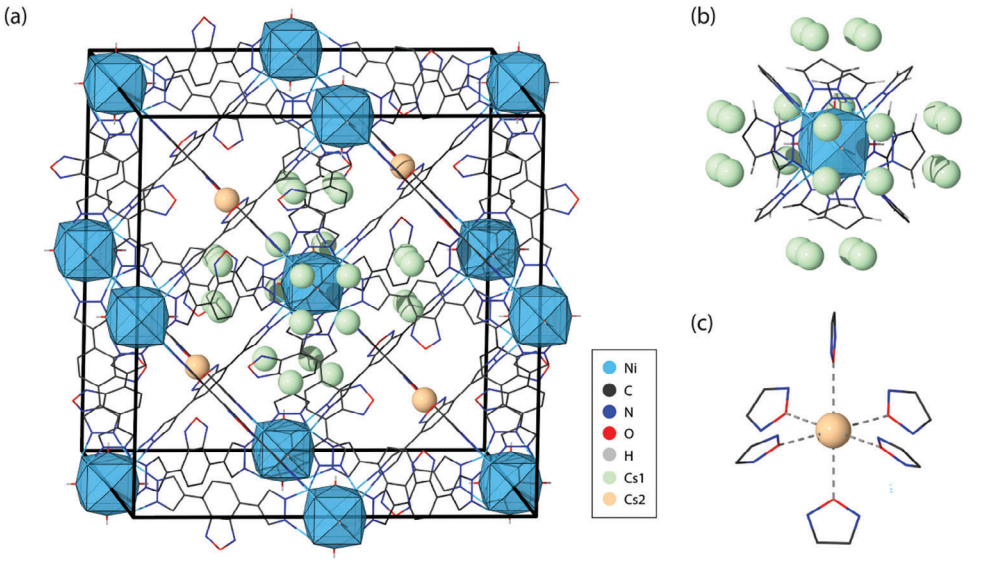

Figure 1. Visualization of $Cs_mCs_n[Ni_8(OH)_6(bpbo)_6]$ (CFA-25_Cs), where m > n and m+n = 2, providing a more intuitive representation of cesium occupancy. (a) Overview of the unit cell. For clarity, the 50/50 disorder of the benzoxadiazole groups has been resolved, and only 24 of the 96 possible Ni_8-SBU coordinating Cs1 positions (green spheres) and 4 of the 8 possible octahedrally coordinated Cs2 positions (orange spheres) are shown. (b) Close-up of Cesium position 1 (Cs1). (c) Close-up of Cesium position 2 (Cs2). Note: The color code and schematic representations for different atoms/groups are embedded in Figure 1 for clarity.

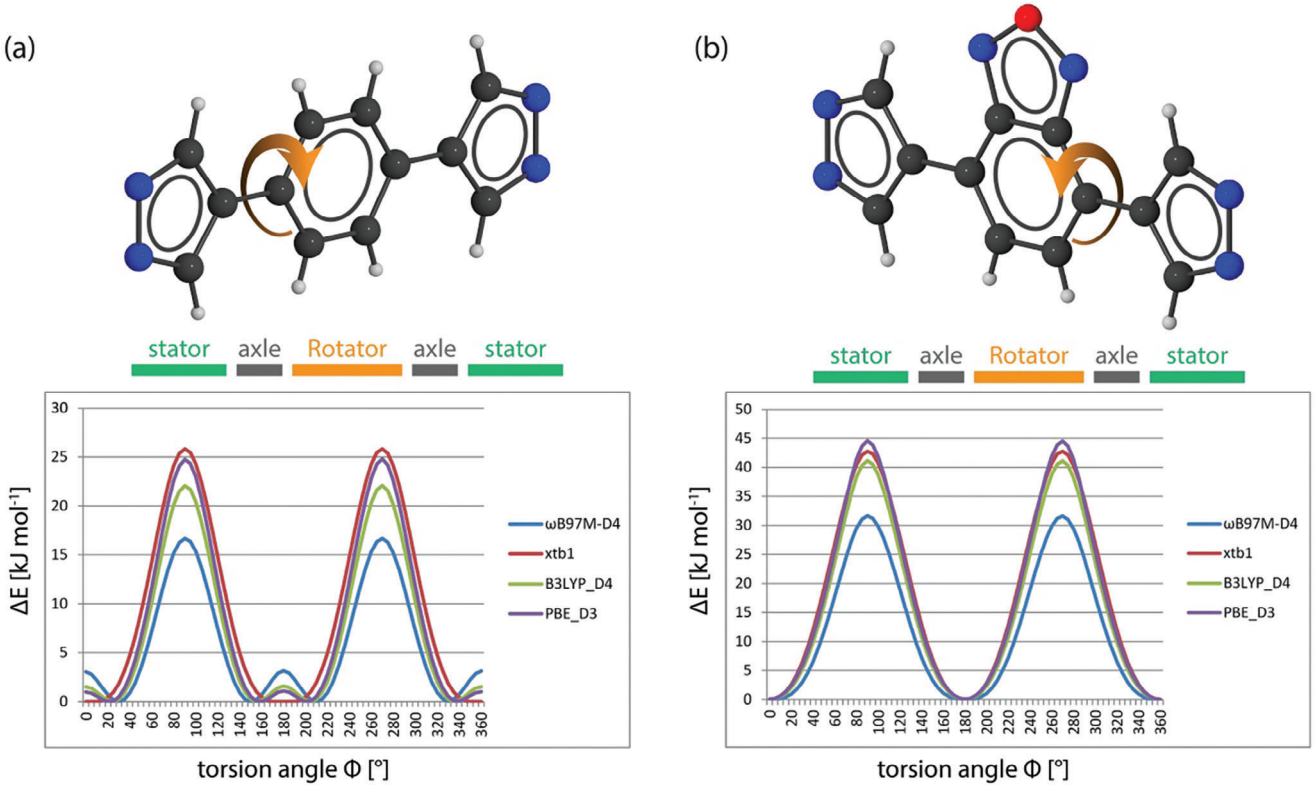

Figure 2. Calculated torsional potential in vacuum as a function of the torsion angle of a) the phenyl unit in BUT-2 and b) the benzoxadiazole unit in CFA-25 using different functionals. (a) shows energy minimums for angles of 25°, 155°, 205°, and 335° (b) for torsion angles of about 0° and 180°.

the framework itself, ions, and other rotor groups. As discussed below, there is a significant electrostatic interaction strength between Cs ions and the polar benzoxadiazole linkers. In the absence of the oxadiazole ring system, the planar arrangement becomes energetically unfavorable, which is often observed for non-functionalized biphenyl and terphenyl systems. Here, symmetric torsional potential energy minima are found at angles deviating ± 25° from 0° (or 180°), leading to a non-coplanar arrangement of the central aromatic ring and pyrazole stators, with this fully confirmed by single crystal structural analysis of BUT-2. The anionic character of the network itself[17] was revealed by detailed DRIFTS studies (Figure S3, Supporting Information). Therefore, similar to the preceding research, it was attempted to replace the charge balancing cations by cesium. By suspending a freshly synthesized sample of $(DMA^+)_2[Ni_8(OH)_6(bpbo)_6]$ in a Cs^+ containing solution with regular exchange of the metal salt solutions, the cations were successfully exchanged (Figure S2, Tables S2 and S3, Supporting Information), yielding the structure $Cs_mCs_n[Ni_8(OH)_6(bpbo)_6]$ (CFA-25_Cs, m+n = 2, Figure S5, Supporting Information). The cesium cations can be located in two different positions in the structure: Besides disordered arrangement around the SBU (Figure 2b), the cesium cations can also be found in an octahedral environment between the benzoxadiazole groups of the organic linkers (Figure 2c). Such a coordination environment is not common for the soft cesium ion, which should not coordinate O donors as hard as the O atom in oxadiazoles, especially since it usually assumes coordination numbers of 8 or more due to its size.[21] Even an exhaustive literature search has yielded only a few hits for octahedrally coordinated Cs, with even these having other coordination partners in the vicinity.[22,23] The Cs-O bond length of 3.241(17) Å found in CFA-25_Cs is in the order of magnitude that can be assumed for Cs complexes, although depending on the coordination number it can vary.[22–24]

Since the synthesis of single crystals always resulted in slight impurities with $Ni(OH)_2$ in the product (Figure S1, Supporting Information), apart for the examinations based on single crystals, the microcrystalline phase-pure product was used for the subsequent studies. Further, both, the microcrystalline product of CFA-25 and CFA-25_Cs were pressed by means of a hydraulic press (also see Figure S2, Supporting Information) and used to investigate the behavior of the networks in dielectric measurements with the goal of answering the different questions.

2.1. Dielectric Spectroscopy

To explore the potential ionic charge transport and reorientational relaxation dynamics of the dipolar linkers in CFA-25_Cs, and to determine the corresponding energy barriers, we have examined this MOF using dielectric spectroscopy. **Figure 3** shows spectra of the dielectric constant ε′ (a), loss ε″ (b), and the real part of the conductivity σ′(c) at selected measurement temperatures. (It should be noted that the latter two quantities are directly related via $\sigma' = \varepsilon''\varepsilon_0\omega$ where ε_0 is the permittivity of vacuum and ω the circular frequency.) Overall, Figure 3 reveals rather complex behavior indicating the superposition of different contributions: The ε′(ν) spectra [Figure 3a] exhibit a succession of two steplike declines with

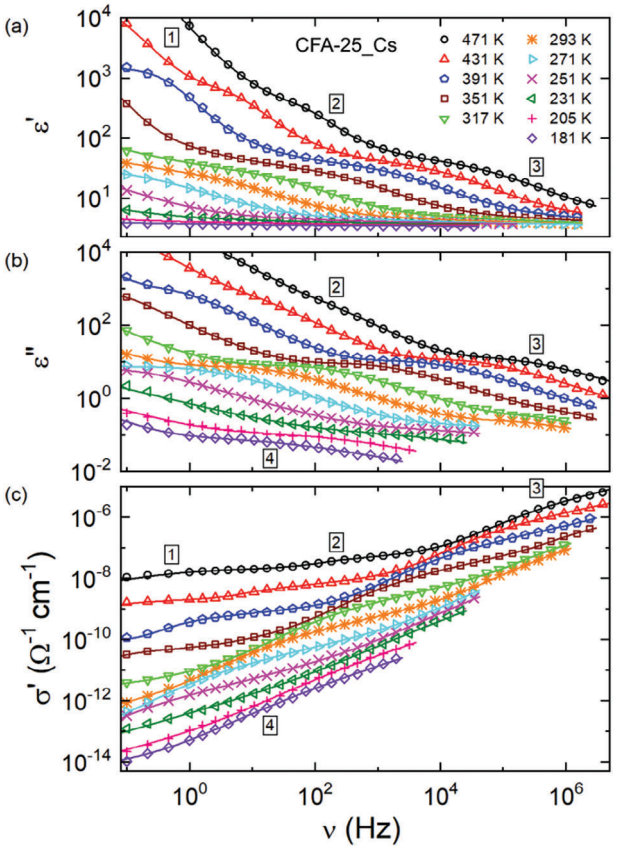

Figure 3. a) Frequency dependence of the dielectric constant, b) loss, and c) conductivity of sample CFA-25_Cs, comprising dipolar linkers, as measured at various temperatures. The lines in (a) and (b) are fits, performed simultaneously for ε′(ν) and ε″(ν) as explained in the text. The lines in (c) were calculated from the fit lines in (b) via the general relation $\sigma' = \varepsilon''\varepsilon_0\omega$. The framed numbers indicate the different processes as discussed in the text (1–3 are indicated for the spectrum at 471 K and 4 denotes the fastest process, revealed at low temperatures only).

increasing frequency (from roughly 10^3 to 30 and from 30 to about 4, in the following denoted process 2 and 3, respectively) which shift to lower frequencies with decreasing temperature. For the two highest temperatures, at frequencies below step 2, ε′(ν) further increases (process 1). While step 2 has shifted out of the frequency window for $T \leq 317$ K, step 3 persists down to lower temperatures and finally is no longer observed below about 231 K. In general, a steplike decrease in ε′(ν) is a signature of a dielectric relaxation process and can be generated by reorientational fluctuations of dipolar entities[24,25] or by interfacial effects which can lead to non-intrinsic, so-called Maxwell-Wagner (MW) relaxations.[26,27] At the points of inflection of the ε′ steps, peaks in ε″(ν) [Figure 3b] are expected. For the relaxation process 2, they show up as rather faint shoulders only, while for the faster process 3, well-pronounced shoulders are revealed. In both cases, the left flanks of the expected peaks are superimposed by the additional contributions at lower frequencies. Finally, at the lowest temperatures, $T \leq 293$K, the appearance of a third shoulder at low ε″ values, of the order of 10^{-1}, indicates another, weak relaxation (process 4; see Figure S7b, Supporting

Information for an enlarged view). The corresponding ε′ step is too small to be detected [Figure S7a, Supporting Information].

In order to interpret these results we first turn to the literature for comparison. For example, processes 1 and 2 are accompanied by the occurrence of very high, so-called "colossal",[28] values of the dielectric constant, ε′ > 1000. According to numerous earlier studies,[26–28] this points to a non-intrinsic, MW-related origin of these features. Such MW relaxations can, for example, arise in polycrystalline samples, such as those investigated here, due to grain boundaries which can act as highly resistive capacitors in series to the bulk sample.[26,28] Moreover, in systems with ionic charge transport, MW relaxations are also commonly found and ascribed to electrode polarization, sometimes termed "blocking electrodes": Here, especially at low frequencies and high temperatures (where ionic mobility is highest), the ions are assumed to arrive at the end of the sample where their motion becomes blocked by the metallic electrode. The formation of a so-called space-charge region then leads to a thin, highly resistive layer at the sample-electrode interface.[27,29] In both cases, large interfacial capacitors are connected in series to the bulk sample. They essentially form a short circuit at high frequencies, leading to the occurrence of a MW relaxation. A commonly-employed equivalent-circuit description of such situations predicts huge apparent values of ε′ at low frequencies.[26–28]

The present MOF contains Cs ions which can be expected to be mobile, and the investigated samples were pressed pellets, involving grain boundaries. Therefore, based on the above discussion, we hypothesize that the spectral features 1 and 2 in Figure 3, leading to colossal ε′ values, can be ascribed to MW relaxations caused by grain boundaries or mobile ions. In section 2.2 we report our theoretical efforts to further corroborate this hypothesis.

In contrast, the upper plateau values of the ε′(ν) steps, related to relaxation process 3, are of order 30 only [Figure 3a]. This is clearly not consistent with MW relaxation, but rather points to an intrinsic, non-interfacial origin. Our hypothesis is therefore that this spectral feature is due to the rotational dynamics of the dipolar benzoxadiazole moieties in the linkers. To check this assignment, we have also measured the reference system BUT-2_Cs, which is isoreticular to CFA-25_Cs but lacks any dipolar rotors in its linkers. **Figure 4** compares dielectric-constant spectra of both MOFs at three identical temperatures. As discussed above, the dipolar system (symbols) reveals the suggested intrinsic relaxation steps (process 3) and, at the highest shown temperature of 431 K, in addition the non-intrinsic MW relaxation 2. In contrast, at the two lowest temperatures the spectra of the reference system (lines) are featureless and ε′(ν) is essentially constant. Only at 431 K, significant frequency dependence shows up for this sample, indicative of a relaxation process. However, it arises at frequencies that are by about four decades lower than for the intrinsic relaxation process of CFA-25_Cs at this temperature and therefore cannot be of the same origin. Obviously, relaxation 3 in CFA-25_Cs is completely absent in BUT-2_Cs, which corroborates the assignment of this process to reorientations of the dipolar linkers, only existing in the former.

As mentioned above, in the loss spectra of Figure 3b, process 3 is revealed by well-pronounced shoulders only, instead of showing clear dielectric loss maxima, ideally expected for dipolar relaxation processes.[21] In conducting materials, it is commonly found that the dc-conductivity contribution to the loss, ε″

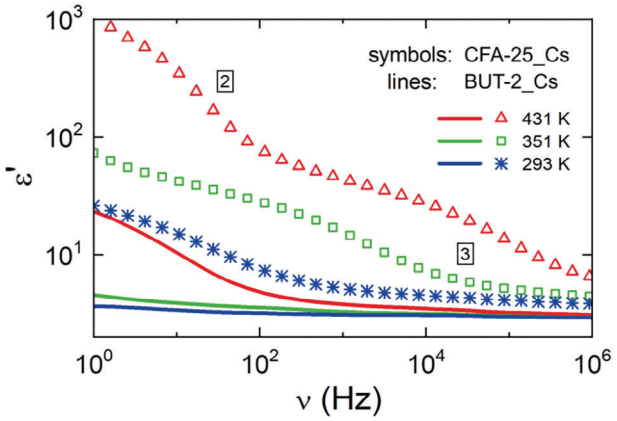

Figure 4. Comparison of dielectric-constant spectra as measured at identical temperatures in sample CFA-25_Cs (with dipolar linkers; symbols) and BUT-2_Cs (without dipolar linkers; lines).

$\propto \sigma_{dc}/\nu$,[21] partly superimposes these loss maxima, especially at low frequencies. In some ionically conducting materials, the loss peaks can become even completely obscured by this effect [see, e.g.,[14,15]]. Due to the rather low conductivity of the investigated MOF, in the present case at least the right flank of the loss peaks and part of the peak plateaus remain visible in the spectra. Anyway, one should be aware that the Kramers-Kronig relation directly connects the real and imaginary parts of the permittivity and, thus, the mentioned occurrence of a steplike decrease with a point of inflection arising in ε′(ν) [Figure 3a] has the same significance for the detection of a relaxation process as a loss peak. Fortunately, the dc conductivity of a material does not contribute to ε′.[21] Therefore, ε′ spectra are unobscured by charge transport and can provide clear evidence for a relaxation process and the corresponding relaxation time, even in materials with high conductivity. The fact that this steplike feature detected for CFA-25_Cs in the real part is completely missing in the isoreticular reference material, which lacks any dipolar linkers (Figure 4), clearly proves the intrinsic dipolar nature of this relaxation process.

Finally, we further corroborate this assignment of process 3 through theoretical simulations discussed in section 2.2.

Currently, we can only speculate about the nature of the detected much slower relaxation process in the reference system: One possibility is a MW relaxation from grain boundaries or electrode polarization, although the upper plateau value of the relaxation is not exceptionally high. Moreover, residual amounts of solvent introduced during sample synthesis or uptake of water within the porous MOF network cannot be excluded. Relaxation processes arising from re-orientational motions of dipolar molecules confined in MOF pores are well known.[30,31] Notably, even at elevated temperature, this process is relatively slow (located at about 1 Hz for 431 K in Figure 4). Thus, interactions of these molecules with the pore walls, slowing down their reorientations,[31,32] could be assumed for this scenario.

If one accepts that process 3 in CFA-25_Cs is of intrinsic nature and reflects the linker-related dipole dynamics, the small faster relaxation 4 revealed in Figure 3b may be tentatively ascribed to a β relaxation process. Such faster relaxations are often observed in dielectric spectra of materials exhibiting glasslike freezing of the re-orientational dynamics upon cooling (we come

back to the glasslike behavior of the present system later).[33,34] In addition to dipolar glass-forming liquids, such rather universal β relaxations are sometimes also found in so-called plastic crystals.[6] In the latter, the centers of gravity of dipolar molecules form a crystalline lattice but these molecules are still able to rotate freely. As mentioned above, in some respects, such systems resemble the present MOF, which is also a crystalline system with dipolar degrees of freedom. The origin of such, so-called, Johari-Goldstein β relaxations[33] is controversial and various explanations were proposed, for example, in terms of dipolar motions within a fine structure of the energy landscape.[35] Interestingly, very recently, part of the present authors also detected such a secondary relaxation process in two carboxylate-based MOFs, featuring linkers with benzothiadiazole moieties, similar to the benzoxadiazole units in the here examined system.[36] As our work focuses on the dipolar-linker dynamics, we refrain here from a more detailed discussion of this fast process.

Due to the above-mentioned direct interrelation of ε'' and σ', the conductivity spectra of Figure 3c in principle contain the same information as the loss spectra of Figure 3b. Nevertheless, the σ' spectra are helpful for visualizing the contributions from charge transport which, in the simplest case, should lead to frequency-independent plateaus in this representation. For the spectra at the three highest temperatures in Figure 3c indeed two such plateaus are seen, for example, below about 10^0 Hz and at $\approx 10^2$ Hz for the 431 K curve (upright triangles). Process 2 occurring at the crossover between these plateaus is of MW nature and can be described by a parallel RC circuit.[26–28] The crossover then essentially arises from the short-circuiting of the corresponding interface (grain boundary or space-charge region) by its capacitance. (This is a somewhat simplified, general explanation for the occurrence of MW relaxations.[26,27]) Then the upper σ' plateau seen at higher frequency corresponds to the intrinsic (bulk) dc conductivity of the sample material. Inspecting Figure 3c directly reveals a strong decrease of this dc plateau upon cooling, indicating thermal activation. It seems reasonable to ascribe the bulk dc conductivity in CFA-25_Cs to charge transport caused by the mobile Cs^+ ions.

The re-orientational dynamics of dipoles can be quantified by their mean relaxation time $\langle\tau\rangle$, which is related to the loss-peak frequency ν_p in $\varepsilon''(\nu)$ and to the point of inflection in $\varepsilon'(\nu)$ by $\langle\tau\rangle \approx 1/(2\pi\nu_p)$.[25] The temperature-dependent shift of the linker-related relaxation features of process 3, revealed in Figure 3, can thus be ascribed to an increase of the relaxation time with decreasing temperature mirroring the slowing down of dipolar motion upon cooling. To obtain quantitative information about the temperature-dependence of the relaxation time in CFA-25_Cs, the spectra of Figure 3a,b were fitted using an equivalent-circuit description for the non-intrinsic MW relaxations (processes 1 and 2 as discussed above). Here the corresponding highly resistive interface layers (e.g., grain boundaries or space-charge regions in case of blocking electrodes) are modeled by parallel RC circuits, connected in series to the bulk sample. This approach is described in detail, for example, in Refs. [26] and. [27] For the suggested intrinsic relaxational contributions to the spectra, the commonly-applied empirical Havriliak-Negami (HN) function was used.[24,37] Finally, the contributions from ionic charge transport were taken into account by assuming a dc conductivity, σ_{dc}, and a power-law ac-conductivity following the so-called universal dielectric response[38] as often found for hopping charge transport.[39] The latter essentially helps to enhance the fit quality at the crossover from the MW relaxation 2 to the intrinsic process 3 but its occurrence is of limited significance. For more details on this approach, see Ref. [36] where part of the present authors described the (significantly lower) conductivity of two carboxylate-based MOFs in this way.

Overall, this approach allows for perfect fits of the data shown in Figure 3. It should be noted that none of these spectra was fitted by simultaneously employing all the different contributions discussed above which would lead to an unreasonably large number of parameters. For example, at the highest temperatures, the β relaxation, process 4, has shifted out of the frequency window and at low temperatures both MW relaxations do no longer contribute. We also want to point out that the determination of the relaxation time of the linker-related intrinsic process 3, the main outcome of this analysis, is only weakly affected by the other contributions because this relaxation leads to well-pronounced steps and shoulders in the ε' and ε'' spectra, respectively (Figure 3). The same holds for the dc conductivity, which is well-defined by the corresponding plateau in $\sigma'(\nu)$ [Figure 3c].

The circles in **Figure 5** show the temperature dependences of the dc conductivity (a) and the mean relaxation time (b) as derived from the fits of the permittivity spectra (Figure 3) using an Arrhenius representation. The conductivity [circles in Figure 5a] reveals linear behavior and thus follows an Arrhenius law,

$$\sigma_{dc} = \sigma_0 \exp\left(\frac{-E_\sigma}{k_B T}\right). \quad (1)$$

The energy barrier E_σ derived from the slope of the linear fit (line drawn through the circles in Figure 5a) is 77 kJ mol^{-1}. Thermally activated charge transport is commonly observed in ionic conductors and it seems likely that the detected conductivity in CFA-25_Cs is due to the interpore diffusion of the Cs cations within the MOF. The found activation energy is of similar order of magnitude as reported for other ionically conducting MOFs.[40] However, one should be aware that the absolute value of the dc conductivity is rather low in the present MOF (e.g., $\sigma_{dc} \approx 1.4 \times 10^{-13}$ Ω^{-1} cm^{-1} at 293 K), indicating that only part of the Cs^+ ions contributes to the conductivity, involving macroscopic charge transport, while the majority is moving only locally at best, for example, between the different CS1 positions located around the SBUs (Figure 1b).

For comparison, the plusses in Figure 5a show σ_{dc} of the reference system BUT-2_Cs. Its absolute values are significantly lower (about 1.5 to 2.5 decades, depending on temperature) than for CFA-25_Cs. Thus, the dipolar linkers in CFA-25_Cs seem to facilitate ionic charge transport and one may speculate about a revolving-door or paddle-wheel mechanism as considered earlier for certain plastic crystals.[8–11,41] However, the interpretation of the ionic conductivity in the present system is not straightforward which is revealed by the fact that, despite its much lower conductivity, the energy barrier in the reference system is somewhat lower (62 versus 77 kJ mol^{-1}). Considering Equation (1), this can be ascribed to its lower pre-exponential factor σ_0 (7.0×10^{-4} Ω^{-1} cm^{-1} for BUT-2_Cs versus 8.0 Ω^{-1} cm^{-1} for CFA-25_Cs). This factor should be determined by the number density of charge carriers and by the attempt frequency. The latter

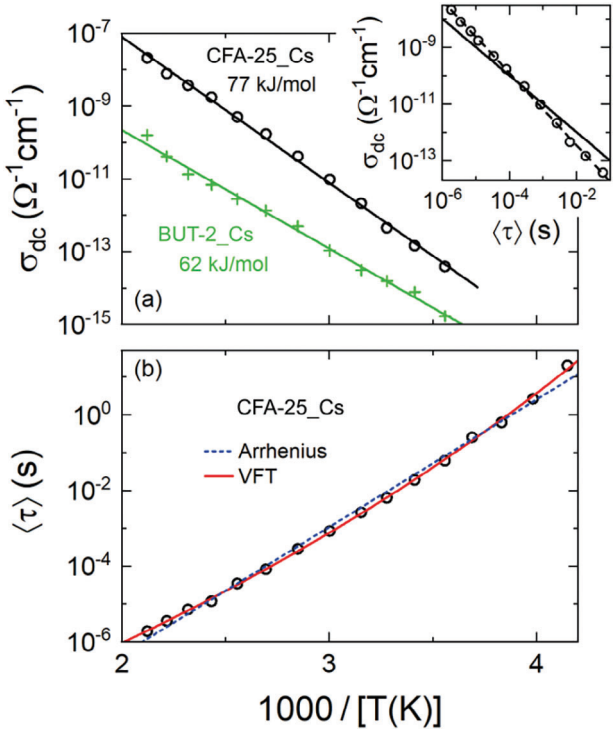

Figure 5. a) Circles: Arrhenius plot of the temperature-dependent dc conductivity of CFA-25_Cs as deduced from the fits in Figure 3. The plusses show the dc conductivity deduced from analogous fits for the reference system BUT-2_Cs. b) Temperature dependence of the mean relaxation time of process 3, ascribed to linker dynamics in CFA-25_Cs, plotted in an Arrhenius-type representation. The data were obtained from the fits shown in Figure 3. The solid line is a fit with the VFT function, Equation (2), leading to $\tau_0 = 4.6 \times 10^{-11}$ s, $D = 46.8$ and $T_{VF} = 87.2$ K. The dashed line shows an alternative linear fit demonstrating weak but significant deviations from Arrhenius temperature dependence. The inset shows σ_{dc} versus $\langle\tau\rangle$ for CFA-25_Cs. The solid line with slope -1 (corresponding to $\sigma_{dc} \propto \langle\tau\rangle^{-1}$ in this double-logarithmic plot) does not fit the experimental data, demonstrating that both quantities are not proportional to each other. The dashed line is a linear fit with slope −1.28.[11]

determines how often the ions "attempt" to overcome the barrier and usually is of the order of typical vibrational frequencies. Obviously, in addition to the enhancement of ionic mobility by the dipole reorientations, other factors also play a role for the higher conductivity in the dipolar system. The inset of Figure 5 confirms that there is no simple, direct coupling of dipolar reorientations and ionic motions: It shows σ_{dc} versus $\langle\tau\rangle$ in a double-logarithmic plot. A slope −1 in this plot (solid line) would indicate a proportionality $\sigma_{dc} \propto \langle\tau\rangle^{-1}$, as reported for various plastic crystals where a revolving-door or paddle-wheel mechanism is assumed to be active.[9,10,41] However, the slope of the linear fit, shown by the dashed line in the inset of Figure 5, is about −1.3, proving that the coupling, if present at all, is more complex.

When assuming simple thermal activation of the reorientational motions of the benzothiadiazole moieties in the linkers, for the temperature dependence of the relaxation time an Arrhenius law, $\langle\tau\rangle \propto \exp[E_\tau/(k_B T)]$, would be expected, too. In Figure 5b, this would correspond to linear behavior where the slope should be proportional to E_τ. However, the experimental data (circles) reveal a continuous curvature which becomes clearly obvious by a comparison with a linear fit (dashed line) showing small, but significant deviations. This finding evidences non-Arrhenius temperature dependence of the relaxation time, a characteristic feature of materials showing glassy freezing,[25,42] including plastic crystals.[6,43,44] For such systems, $\tau(T)$ is commonly fitted by the empirical Vogel-Fulcher-Tammann (VFT) function, which we employ here in a slightly modified form proposed by Angell.[45]

$$\langle\tau\rangle = \tau_0 \exp\left[\frac{DT_{VF}}{T - T_{VF}}\right] \quad (2)$$

Here τ_0 is an inverse attempt frequency and T_{VF} is the Vogel-Fulcher temperature, where $\langle\tau\rangle$ diverges. D is the so-called strength parameter, providing a quantitative measure of the deviations from Arrhenius behavior (large D corresponds to small deviations[45]). As shown by the solid line in Figure 5b, Equation (2) enables a good description of the experimental $\tau(T)$ data.

The increasing slope revealed by $\log\tau(1/T)$ in the Arrhenius plot of Figure 5b upon cooling, which is typical for VFT behavior, can be essentially seen as increase of the effective energy barrier governing dipolar rotations. In glass formers, this is nowadays commonly ascribed to a continuous increase of the cooperativity of molecular motion upon cooling, considered as a characteristic property of glassy freezing.[46,47] Cooperativity means that the molecules "collectively rearrange over some length scale"[47] as originally suggested by the Adam-Gibbs theory of the glass transition.[48] The growth of this length scale then explains the observed increase of the effective energy barrier upon cooling.

While the VFT equation was originally developed for glass-forming liquids, its applicability is also well established for systems showing glassy freezing of non-structural degrees of freedom. This includes the above-mentioned plastic crystals, whose molecules are located on a crystalline lattice but still can rotate.[6,43,44] This rotation dynamics, which is fast at high temperatures, often exhibits glassy freezing upon cooling, that is, it continuously slows down over many decades until the rotation essentially ceases below an orientational glass-transition temperature, defined by $\langle\tau\rangle(T_g^o) \approx 100$ s. Cooperativity was also invoked for this class of materials to rationalize their non-Arrhenius behavior.[49] As mentioned above, the present MOF, featuring re-orientational dipolar motions in a crystalline lattice, in some respects resembles plastic crystals. Therefore, the non-Arrhenius behavior evidenced by Figure 5b can be ascribed to cooperativity between the rotating dipoles. The latter can have different origins, for example, steric effects or direct dipole-dipole interactions. Similar conclusions were drawn for two carboxylate-based MOFs, featuring linkers with benzothiadiazole units.[36] From the strength parameter $D = 46.8$, obtained from the VFT fit of $\tau(T)$ in Figure 5b, the so-called fragility m can be derived.[50] It is the most common quantity for quantifying deviations from Arrhenius behavior. The resulting $m = 28.6$ implies rather moderate deviations from Arrhenius behavior,[50] as also found for the previously investigated MOFs with benzothiadiazole units[36] and for most plastic crystals.[6,43] In analogy to glass-forming liquids and plastic crystals, one can use the definition $\langle\tau\rangle(T_g^o) \approx 100$ s to deduce an orientational glass-transition temperature T_g^o of CFA-25_Cs from

the VFT fit. This leads to $T_g^o \approx 231$ K. Below this temperature, the rotational motion of the benzothiadiazole units essentially is frozen and their orientations are disordered, representing a kind of "orientational glass" state.

The computational calculations of the present work provide an estimate of the rotational energy barriers sensed by single dipolar units in CFA-25_Cs. However, they cannot account for the cooperative inter-dipole interactions that give rise to the VFT behavior of $\tau(T)$ as observed by dielectric spectroscopy [Figure 5b]. To facilitate the direct comparison of the computational and dielectric results, the energy barrier E_s that would be detected without any cooperativity can be estimated from the obtained VFT parameters: It is commonly assumed that cooperativity becomes less important for the dipolar motions at high temperatures and vanishes for $T \rightarrow \infty$. This is due to the fact that, at very high temperatures, any cooperative inter-dipole interactions can be neglected, compared to the dominant thermal energy $k_B T$. Indeed, Equation (2) crosses over into Arrhenius behavior for $T \rightarrow \infty$, and the energy barrier (in K) then is given by $E_s = DT_{VF} \approx 4081$ K. This leads to a single-dipole rotational energy barrier of 34 kJ mol^{-1} for CFA-25_Cs.

2.2. Theoretical Calculations

To confirm the different assumptions based on the dielectric spectroscopy measurements, a number of theoretical calculations were conducted. First, the rotational barrier of the organic linkers was investigated. Depending on the DFT functional used, simulated values of about 30–45 kJ mol^{-1} were obtained for CFA-25 (Figure 2b), and about 15–25 kJ mol^{-1} for BUT-2 (Figure 2a). Errors between the different functionals, at least for rotational barriers, thus seem to range between 10 and 15 kJ mol^{-1}. We expect the errors for our nudged elastic band calculations of Cs migration barriers (see below) to lie in a similar range, at a minimum. The former rotational barrier computed with the highly accurate ωB97M-D4[51] functional agrees very well with the experimentally obtained value of about 34 kJ mol^{-1} for CFA-25.

In a second step, the dynamics of the Cs cations between two unit cells were considered. Cesium can occupy two positions within the network, as noted at the beginning (cf. Figure 1). Which of the two positions is energetically more favorable for charge transport is not immediately obvious. On the one hand, there is an attractive coordination environment for the Cs1 position due to the large distribution of charge on the SBU as well as the soft properties of the Cs cation itself; on the other hand, the octahedral coordination of the cesium cations in the Cs2 position should be energetically very attractive. However, for Cs2 it could be assumed that the charge transport is enhanced by the thermally excited rotation of the dipolar groups and a coherent transport mechanism analogous to the 'paddle wheel' or 'revolving door' principle may occur: Within this scenario, the dipolar groups rotate thermally activated and facilitate the transport of the Cs cations to the next octahedral gap. However, the dielectric results (cf. inset of Figure 5) speak against such a direct coupling of dipolar re-orientational and ionic translation dynamics. This observation suggests a possible simplification of our simulations. Focusing here on ion transport barriers, such external electric fields could potentially influence the results by changing the rotation of the dipolar groups. Yet, given that those two motions appear to be independent, we can approximate the barrier in field-free simulations.

Interestingly, the transport between the Cs1 positions of neighboring unit cells is the energetically more attractive pathway. Even though the rotational barrier of the organic linker per se is far below the energies necessary for charge transport between the Cs1 positions, the octahedral arrangement of the ligands around the Cs cations in the Cs2 position seems to be energetically so favorable that it can only be broken by applying very high energies. To illustrate this, we conducted a series of high-temperature (T = 1000 K) Monte Carlo simulations of Cs movement in both BUT-2 and CFA-25 in their respective conventional unit cells. The resulting Cs probability distributions are depicted in **Figure 6**a for BUT-2 and Figure 6b,c for CFA-25. In each case, the probability distribution iso-surfaces show a connected network through all pores. Figure 6 also depicts local minima and transition states for the Cs transition from one site to another, with the respective points found by a brute force search in the 3D probability distribution. Having identified minima and transition states allows us to estimate free energy differences for these processes. For all three pathways depicted in Figure 6 we find quite similar barriers (a: 66.8 kJ mol^{-1}, b: 65.1 kJ mol^{-1}, c: 67.4 kJ mol^{-1}). They are of similar magnitude as those deduced from the dielectric experiments (cf. Figure 5a). The barrier for path b is inverted in the sense that the energy cost of going from the Cs2 site to the transition state is much higher (65.1 kJ mol^{-1}) than the one going from the vicinity of the metal centers to the transition state (22.0 kJ mol^{-1}) owing to the stabilization of the octahedral Cs2 site due to the polar rotors. Note that this estimate neglects framework degrees of freedom and thus potentially overestimates the barriers to and from the Cs2 site. At the same time the high sampling temperature—chosen to accurately sample the transition states—leads to an overestimation of entropic contributions to the computed free energy barriers. These effects do not fully cancel each other out as illustrated by the relatively small barriers found for the diffusion from the Cs2 site. As a comparison, we computed the binding energy of the Cs cation at the Cs2 position using PBE-DFT-D3 and a cluster model, to avoid finite size effects due to the removal of a charged ion. Specifically, we computed the energy difference between a (hydrogen-saturated) cluster of the six polar linkers, with and without the Cs ion as E_{bind} = E(linkers+Cs)-E(linkers)-E(Cs). Indeed, we found the octahedral coordination to stabilize the Cs2 position by E_{bind} = 172.1 kJ mol^{-1}, exceeding by far the computed free energy barriers for Cs diffusion as computed from the Cs probability distribution. Also, comparing to Figure 5, we find the binding energy to surpass barriers to the rotation of individual linkers, hinting against a possible shuttling mechanism by the polar linkers to and from the Cs2 position.

Thus, the ions at the Cs1 position seem to be the most likely candidates for the observed ionic conductivity. Therefore, we explored two symmetry inequivalent pathways only involving Cs1 positions using the Nudged Elastic Band method in the MOFs periodic cell. To this end, we again employed PBE-DFT-D3 energetics. Such computed energy pathways, depicted as path 1 and path 2 in **Figure 7**, show barriers of 155 and 61 kJ mol^{-1}, respectively. Note that in both cases, the Cs ion does not migrate through the empty center of the pore, but rather along the linkers to optimize

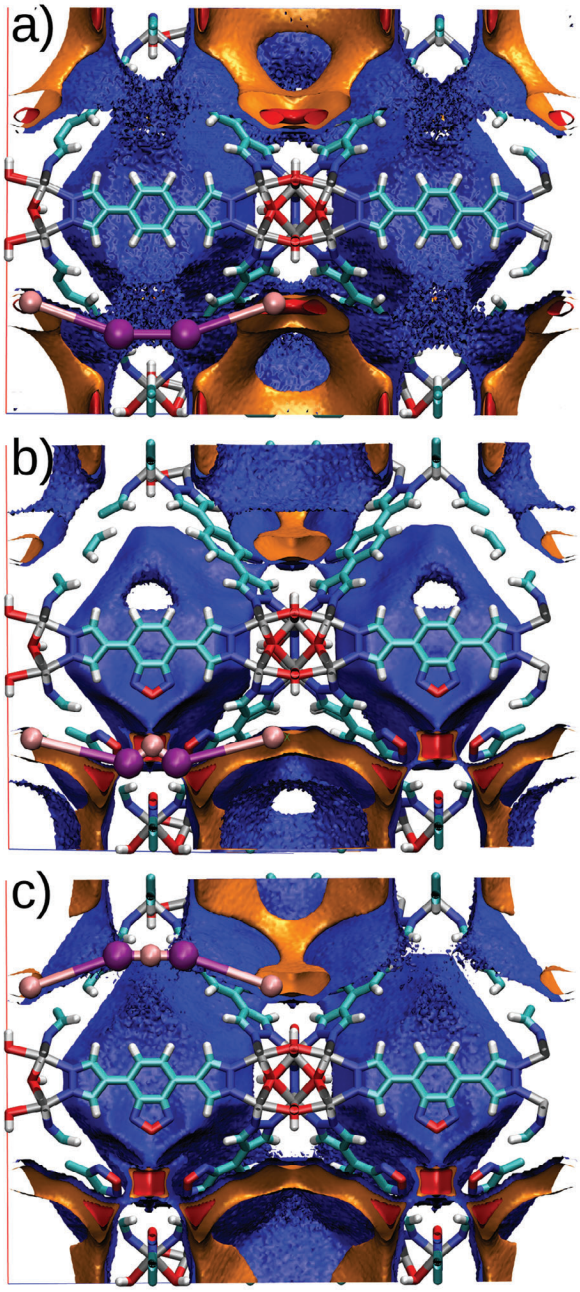

Figure 6. Probability distribution functions of the Cs ion position in the a) BUT-2 and b,c) CFA-25 structures. Plotted are three iso-values: red (a: 0.5, b: 10^{-2}, c: 10^{-2}), orange (a: 0.05, b: 10^{-3}, c: 10^{-3}), and blue (a: 10^{-6}, b: 10^{-4}, c: 10^{-6}), isovalues were chosen for illustration purposes for each pathway. Minimum energy pathways are highlighted in ball and stick format with purple spheres indicating transition states and pink spheres the respective (meta-)stable positions.

dispersion interactions. While this brings the migrating Cs closer to the pinned Cs in the Cs2 position, Coulomb repulsion seems to be mostly screened by the linkers surrounding this cation.

In summary, based on the theoretical calculations, the experimentally obtained values can be confirmed and the following two observations can be made: First, the rotation of the rotators in the organic linkers can be excited with an energy of about 30–45 kJ mol^{-1} (in accord with the dielectric result of 34 kJ mol^{-1}), but only for those that are not involved in the octahedral coordination of the Cs cations in the Cs2 position. On the other hand, charge transport of the Cs cations through the pores of the MOF can be excited, with this taking place between the Cs1 positions.

3. Conclusion

Overall, in our study the molecular dynamics of CFA-25_Cs were examined in detail, first by dielectric spectroscopy, and second by quantum mechanical calculations. Through experimental studies, two dynamical processes were observed, one being the rotation of the rotators of the organic linkers, and the other being the charge transport of the Cs cations. By means of theoretical calculations it was found that only those rotators can be rotated which are not involved in the octahedral coordination of the Cs cations in the Cs2 position and that the charge transport of the Cs cations through the porous network occurs preferentially between the Cs1 positions. The experimentally derived energy barriers for both dynamics are in reasonable agreement with the theoretical calculations. Our findings provide crucial insights into the interplay between dipolar dynamics and ionic transport in MOF systems. The experimental observations, corroborated by theoretical simulations, suggest that while dipolar reorientations occur, they are in contrast to various plastic crystalline ionic conductors not directly coupled to ionic motion via a revolving door mechanism, as initially hypothesized. Instead, we observe a more complex relationship where dipolar reorientation may indirectly influence conductivity. These results advance the understanding of MOF-based ionic conductors and suggest pathways for optimizing their performance in energy-related applications, such as solid-state electrolytes.

4. Experimental Section

Materials: Chemicals and reagents were purchased from commercial suppliers and used as received.

1,4-Bis(1H-pyrazol-4-yl)benzoxadiazole (H_2bpbo): H_2bpbo was synthesized according to literature.[52]

Synthesis of $(DMA^+)_2[Ni_8(OH)_6(bdp)_6]$ (BUT-2)[16]: Microcrystalline product was obtained by reacting $Ni(AcO)_2 \bullet (H_2O)_4$ (33.0 mg; 0.13 mmol) dissolved in 2.4 mL water and H_2bdp (21.0 mg; 0.10 mmol) dissolved in 3 mL DMAc in a 25 mL autoclave with Teflon inlay overnight at 135 °C in an oven. The resulting turquoise solid was filtered off and washed with DMAc, water, and ethanol and then dried under vacuum. Yield: 78 %.

IR bands (cm^{-1}): 3642 (s), 3378 (br), 3107 (w), 3028 (w), 2323 (w), 2050 (w), 1981 (w), 1616 (w), 1575 (s), 1470 (w), 1351 (m), 1248 (s), 1168 (m), 1128 (m), 1052 (s), 960 (s), 819 (s), 800 (s), 678 (s), 650 (s), 532 (s), 503 (s).

Synthesis of $Cs_2[Ni_8(OH)_6(bdp)_6]$ (BUT-2_Cs): BUT-2_Cs was obtained by suspending BUT-2 in 0.05 M $CsOH \bullet (H_2O)$ solution (ethanol 50:50 water; v/v) with multiple exchanges of the salt solution over a 24 h period followed by filtration and washing with water and ethanol and drying under vacuum. Yield: 100 %.

IR bands (cm^{-1}): 3642 (s), 3381 (br), 3107 (w), 3029 (w), 2359 (w), 2050 (w), 1969 (w), 1616 (w), 1574 (s), 1457 (w), 1350 (m), 1248 (s), 1167 (m), 1128 (m), 1052 (s), 960 (s), 820 (s), 800 (s), 679 (s), 650 (s), 533 (s), 503 (s).

Synthesis of $(DMA^+)_2[Ni_8(OH)_6(bpbo)_6]$ (CFA-25): The following reaction conditions allow obtaining single crystals >100 µm, however,

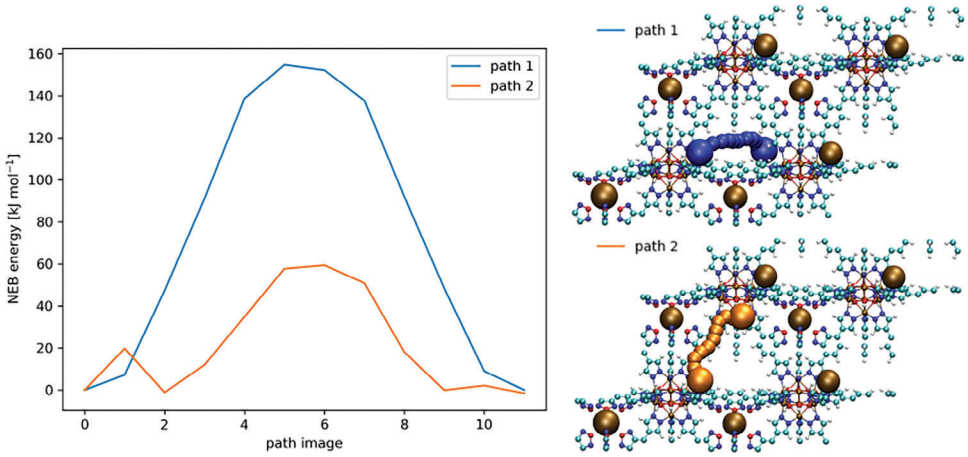

Figure 7. Left, Energy profiles of the two Cs migration pathways. Path 1 investigates a migration from the Cs1 site in the main simulation cell to another cell, while path 2 follows the Cs from one metal center to another in the same cell. Right, illustration of the two pathways, highlighted as small spheres placed at the final NEB image positions. Initial and final positions are highlighted with larger spheres, other Cs cations are depicted as brown spheres.

$Ni(OH)_2$ was formed as a by-product: $Ni(NO_3)_2{\bullet}(H_2O)_6$ (29.0 mg; 0.10 mmol) was dissolved in 3.7 mL of water and mixed with H_2bpbo (12.5 mg; 0.05 mmol) dissolved in 3 mL of DMAc in a 25 mL autoclave with Teflon inlay and then heated to 160 °C for 3 d under solvothermal conditions in an oven. The resulting dark red crystals were filtered off and washed with DMAc, water, and ethanol and then dried under vacuum. Yield: 85 %.

In order to obtain a phase-pure product, the water-DMAc ratio was lowered, resulting in strong intergrowth of the crystals: $Ni(NO_3)_2{\bullet}(H_2O)_6$ (29.0 mg; 0.10 mmol) was dissolved in 1.5 mL of water and mixed with H_2bpbo (12.5 mg; 0.05 mmol) dissolved in 3 mL of DMAc in a 25 mL autoclave with Teflon inlay and then heated to 160 °C for 3 d under solvothermal conditions in an oven. The resulting dark red crystals were filtered off and washed with DMAc, water, and ethanol and then dried under vacuum. Yield: 79 %.

Microcrystalline product was obtained by reacting $Ni(AcO)_2{\bullet}(H_2O)_4$ (33.0 mg; 0.13 mmol) dissolved in 2.4 mL water and H_2bpbo (25.1 mg; 0.10 mmol) dissolved in 3 mL DMAc in a 25 mL autoclave with Teflon inlay overnight at 135 °C in an oven. The resulting dark red solid was filtered off and washed with DMAc, water, and ethanol and then dried under vacuum. Yield: 81 %.

IR bands (cm^{-1}): 3640 (s), 3380 (br), 2970 (w), 2323 (w), 2111 (w), 2050 (w), 1980 (w), 1606 (s), 1557 (s), 1469 (w), 1398 (m), 1373 (m), 1321 (m), 1251 (s), 1174 (m), 1071 (s), 1034 (s), 1009 (m), 926 (s), 894 (w), 864 (w), 839 (s), 794 (br), 665 (s), 621 (s), 589 (w), 546 (s), 507 (br), 467 (s).

Synthesis of $Cs_2[Ni_8(OH)_6(bpbo)_6]$ (CFA-25_Cs): CFA-25_Cs was obtained by suspending CFA-25 in 0.05 M $CsOH{\bullet}(H_2O)$ solution (ethanol 50:50 water; v/v) with multiple exchanges of the salt solution over a 24 h period followed by filtration and washing with water and ethanol and drying under vacuum. Yield: 100 %.

IR bands (cm^{-1}): 3641 (s), 2323 (w), 2050 (w), 1979 (w), 1606 (s), 1558 (s), 1397 (m), 1373 (m), 1321 (m), 1251 (s), 1173 (m), 1071 (s), 1034 (s), 1008 (m), 927 (s), 895 (w), 863 (w), 839 (s), 798 (br), 665 (s), 622 (s), 589 (w), 546 (s), 506 (br), 467 (s).

Activation of MOF Samples: The MOF samples were activated by subjecting them to heating at 180 °C under vacuum for 12 h. This process ensured the removal of residual solvents and gases from the pores, allowing for optimal performance during subsequent measurements and analyses.

Preparation of pellets for DES Measurements: Pellets were obtained by pressing ≈5 mg of the respective samples under a pressure of 5 t for 5 min. Continued crystallinity was ensured by powder X-ray diffraction.

Powder X-ray Diffraction: X-ray powder diffraction (PXRD) data were collected in the 4–40° 2θ range using a Seifert XRD 3003 TT–powder diffractometer with a Meteor1D detector operating at room temperature using Cu $K\alpha_1$ radiation ($\lambda = 1.54187$).

Single Crystal X-ray Diffraction: Single crystal X-ray diffraction measurements were conducted by mounting a single crystal on a MiTeGen MicroMount and collecting the X-ray reflection data set using a Bruker D8 Venture diffractometer. Intensity measurements were carried out using monochromatic (doubly curved silicon crystal) Mo K_α radiation (0.71073 Å) emitted from a sealed microfocus tube with generator setting of 50 kV and 1 mA. Integrated intensities and unit cell refinements were performed using the Bruker SAINT software package. The structures were solved by direct methods and refined using the SHELXL 2018/3 program.[53]

EDX Measurements: Energy-dispersive X-ray spectroscopy (EDX) measurements were made using a Zeiss Crossbeam 550 scanning electron microscope equipped with an EDAX SiLi detector with an operating voltage of 20 kV.

Dielectric Spectroscopy: Prior to the dielectric measurement, the samples were dried under vacuum at 100 °C for 2.5 h. The disc-shaped sample pellets (thickness ≈0.3 mm) were contacted with colloidal graphite on opposite sides, leading to a parallel-plate capacitor geometry with sample areas of about 10 mm^2. All measurements were performed in a Quatro cryosystem by Novocontrol in a steady stream of dry N_2-gas, employing a frequency-response Alpha-A analyzer by Novocontrol using pseudo-fourpoint contact geometry. The samples were investigated in a broad frequency range from 0.1 Hz to about 4 MHz between 180 and 470 K. At very low sample conductances and high frequencies, the experimental errors specified for the device can become high, leading to systematic deviations and unreliable results. To avoid confusion, these regions are omitted in the shown spectra.

DFT Calculations: Rotational barriers were estimated with the ORCA code with TightSCF convergence criteria. For tight binding GFN1-xtb D3 calculations this work employed standard basis set settings, while for the respective DFT calculations this work used def2-TZVPP basis functions. All other DFT calculations were performed with the CP2K program package[54] using the DZVP-MOLOPT-GTH basis set and the standard Gödecker-Teter-Hutter pseudopotentials. Unless mentioned explicitly otherwise, exchange and correlation were treated with the PBE functional[55] and dispersion interactions were accounted for using the D3-scheme.[56] This work employed the nudged elastic band method with 12 images connected by strings with a spring constant of k = 0.05 Hartree/Bohr. The geometry of each image was optimized until residual forces fell below 0.001 Hartree/Bohr.

Classical Calculations: All classical simulations were performed with the raspa2 program package[57] and the universal force field (UFF).[58] The necessary charge models were obtained using the REPEAT method[20]

from PBE-DFT-D3 computed electron densities. Raspa2 particle insertion Monte Carlo simulations were performed in the conventional cell, a 2 × 2 × 2 unit cell and limited to in total 8 Cs ions. For technical and efficiency reasons, framework degrees of freedom were frozen and only Cs ions were moved. This work performed in total 250 million steps each for BUT-2 and CFA-25, at an ionic temperature of 1000 K to ensure sampling of the barrier regions.

[CCDC 2282551–2282552 contains the supplementary crystallographic data for this paper. These data can be obtained free of charge from The Cambridge Crystallographic Data Centre via https://www.ccdc.cam.ac.uk/data_request/cif.]

Supporting Information

Supporting Information is available from the Wiley Online Library or from the author.

Acknowledgements

The authors are grateful for financial support from DFG grants VO-829/12-2 and OB-425/3-2 (DFG Priority Program 1928 "Coordination Networks: Building Blocks for Functional Systems COORNETs")

Open access funding enabled and organized by Projekt DEAL.

Conflict of Interest

The authors declare no conflict of interest.

Data Availability Statement

The data that support the findings of this study are available from the corresponding author upon reasonable request.

Keywords

cs cation, dipolar group, ion transport, ionic conductivity, metal-organic framework, molecular dynamics, rotational motion

Received: August 21, 2024
Revised: October 15, 2024
Published online:

[1] a) H.-C. Zhou, J. R. Long, O. M. Yaghi, *Chem. Rev.* **2012**, *112*, 673; b) H. Furukawa, K. E. Cordova, M. O'Keeffe, O. M. Yaghi, *Science* **2013**, *341*, 1230444.

[2] a) D. Sun, W. Liu, M. Qiu, Y. Zhang, Z. Li, *Chem. Commun.* **2015**, *51*, 2056; b) O. M. Yaghi, M. J. Kalmutzki, C. S. Diercks, *Introduction to Reticular Chemistry. Metal-Organic Frameworks and Covalent Organic Frameworks*, Wiley-VCH, Weinheim, **2019**; c) H. Jiang, D. Alezi, M. Eddaoudi, *Nat. Rev. Mater.* **2021**, *6*, 466.

[3] a) M. Kalaj, S. M. Cohen, *ACS Cent. Sci.* **2020**, *6*, 1046; b) S. Mandal, S. Natarajan, P. Mani, A. Pankajakshan, *Adv. Funct. Mater.* **2021**, *31*, 2006291; c) R. Freund, O. Zaremba, G. Arnauts, R. Ameloot, G. Skorupskii, M. Dincă, A. Bavykina, J. Gascon, A. Ejsmont, J. Goscianska, M. Kalmutzki, U. Lachelt, E. Ploetz, C. S. Diercks, S. Wuttke, *Angew. Chem. Int. Ed. Engl.* **2021**, *60*, 23975.

[4] a) P. Ji, X. Feng, P. Oliveres, Z. Li, A. Murakami, C. Wang, W. Lin, *J. Am. Chem. Soc.* **2019**, *141*, 14878; b) M. Moayed Mohseni, M. Jouyandeh, S. Mohammad Sajadi, A. Hejna, S. Habibzadeh, A. Mohaddespour, N. Rabiee, H. Daneshgar, O. Akhavan, M. Asadnia, M. Rabiee, S. Ramakrishna, R. Luque, M. Reza Saeb, *Chem. Eng. J.* **2022**, *449*, 137700; c) C.-W. Kung, K. Otake, C. T. Buru, S. Goswami, Y. Cui, J. T. Hupp, A. M. Spokoyny, O. K. Farha, *J. Am. Chem. Soc.* **2018**, *140*, 3871; d) D. Sheberla, J. C. Bachman, J. S. Elias, C.-J. Sun, Y. Shao-Horn, M. Dincă, *Nat. Mater.* **2017**, *16*, 220; e) R. Freund, U. Lächelt, T. Gruber, B. Rühle, S. Wuttke, *ACS Nano* **2018**, *12*, 2094.

[5] A. Singhania, S. Kalita, P. Chettri, S. Ghosh, *Nanoscale Adv.* **2023**, *5*, 3177.

[6] R. Brand, P. Lunkenheimer, A. Loidl, *J. Chem. Phys.* **2002**, *116*, 10386.

[7] a) P.-J. Alarco, Y. Abu-Lebdeh, A. Abouimrane, M. Armand, *Nat. Mater.* **2004**, *3*, 476; b) S. Kim, H. Oguchi, N. Toyama, T. Sato, S. Takagi, T. Otomo, D. Arunkumar, N. Kuwata, J. Kawamura, S.-I. Orimo, *Nat. Commun.* **2019**, *10*, 1081; c) J. M. Pringle, *Phys. Chem. Chem. Phys.* **2013**, *15*, 1339.

[8] D. R. MacFarlane, M. Forsyth, *Adv. Mater.* **2001**, *13*, 957.

[9] K. Geirhos, P. Lunkenheimer, M. Michl, D. Reuter, A. Loidl, *J. Chem. Phys.* **2015**, *143*, 81101.

[10] D. Reuter, P. Lunkenheimer, A. Loidl, *J. Chem. Phys.* **2019**, *150*, 244507.

[11] E. Cooper, C. Angell, *Solid State Ionics* **1986**, *18*, 570.

[12] a) R. Aronsson, B. Jansson, H. E. G. Knape, A. Lundén, L. Nilsson, C.-A. Sjöblom, L. M. Torell, *J. Phys. Colloques* **1980**, *41*, C6. b) Z. Zhang, L. F. Nazar, *Nat. Rev. Mater.* **2022**, *7*, 389.

[13] Z.-H. Jia, J.-Y. Liu, D.-X. Liu, S.-Y. Zhang, Z.-Y. Du, C.-T. He, W.-X. Zhang, X.-M. Chen, *J. Mater. Chem. C* **2021**, *9*, 8076.

[14] D. Reuter, C. Binder, P. Lunkenheimer, A. Loidl, *Phys. Chem. Chem. Phys.* **2019**, *21*, 6801.

[15] P. Sippel, S. Krohns, D. Reuter, P. Lunkenheimer, A. Loidl, *Phys. Rev. E* **2018**, *98*, 052605.

[16] Y.-Z. Zhang, T. He, X.-J. Kong, Z.-X. Bian, X.-Q. Wu, J.-R. Li, *ACS Mater. Lett.* **2019**, *1*, 20.

[17] R. Freund, A. Kalytta-Mewes, M. Kraft, D. Volkmer, *Chem. Commun.* **2022**, *58*, 9349.

[18] J. Lu, H. Zhang, J. Hou, X. Li, X. Hu, Y. Hu, C. D. Easton, Q. Li, C. Sun, A. W. Thornton, M. R. Hill, X. Zhang, G. Jiang, J. Z. Liu, A. J. Hill, B. D. Freeman, L. Jiang, H. Wang, *Nat. Mater.* **2020**, *19*, 767.

[19] a) F. L. Tobiason, L. Huestis, C. Chandler, S. E. Pedersen, P. Peters, *J. Heterocycl. Chem.* **1973**, *10*, 773; b) J. Wudarczyk, G. Papamokos, V. Margaritis, D. Schollmeyer, F. Hinkel, M. Baumgarten, G. Floudas, K. Müllen, *Angew. Chem. Int. Ed. Eng.* **2016**, *55*, 3220; c) F. Šembera, J. Plutnar, A. Higelin, Z. Janoušek, I. Císařová, J. Michl, *Inorg. Chem.* **2016**, *55*, 3797.

[20] C. Campañá, B. Mussard, T. K. Woo, *J. Chem. Theory Comput.* **2009**, *5*, 2866.

[21] R. G. Pearson, *J. Am. Chem. Soc.* **1963**, *85*, 3533.

[22] B. Sun, Y. Zhao, J.-G. Wu, Q.-C. Yang, G.-X. Xu, *J. Mol. Struct.* **1998**, *471*, 63.

[23] E. Freisinger, A. Schneider, M. Drumm, A. Hegmans, S. Meier, B. Lippert, *J. Chem. Soc. Dalton Trans.* **2000**, 3281, https://pubs.rsc.org/en/content/articlelanding/2000/dt/b004906i.

[24] F. Kremer, A. Schönhals, *Broadband Dielectric Spectroscopy*, Springer, Berlin, Germany **2003**.

[25] P. Lunkenheimer, A. Loidl, in *The Scaling Of Relaxation Processes* (Eds: F. Kremer, Ed., A. Loidl), Springer, Cham, Germany **2018**.

[26] P. Lunkenheimer, S. Krohns, S. Riegg, S. G. Ebbinghaus, A. Reller, A. Loidl, *Eur. Phys. J. Spec. Top.* **2009**, *180*, 61.

[27] S. Emmert, M. Wolf, R. Gulich, S. Krohns, S. Kastner, P. Lunkenheimer, A. Loidl, *Eur. Phys. J. B* **2011**, *83*, 157.

[28] P. Lunkenheimer, V. Bobnar, A. V. Pronin, A. I. Ritus, A. A. Volkov, A. Loidl, *Phys. Rev. B* **2002**, *66*, 052105.

[29] J. C. Dyre, P. Maass, B. Roling, D. L. Sidebottom, *Rep. Prog. Phys.* **2009**, *72*, 046501.

[30] a) S. Balčiūnas, M. Šimėnas, D. Pavlovaitė, M. Kinka, F.-K. Shieh, K. C.-W. Wu, J. Banys, R. Grigalaitis, *J. Phys. Chem. C* **2019**, *123*, 631; b) J. K. H. Fischer, P. Sippel, D. Denysenko, P. Lunkenheimer, D. Volkmer, A. Loidl, *J. Chem. Phys.* **2015**, *143*, 154505; c) J. K. H. Fischer, P. Sippel, D. Denysenko, P. Lunkenheimer, D. Volkmer, A. Loidl, *Commun. Phys.* **2020**, *3*, 95.
[31] M. Uhl, J. K. H. Fischer, P. Sippel, H. Bunzen, P. Lunkenheimer, D. Volkmer, A. Loidl, *J. Chem. Phys.* **2018**, *150*, 024504.
[32] M. Arndt, R. Stannarius, W. Gorbatschow, F. Kremer, *Phys. Rev. E, Stat. Phys. Plasmas Fluids Relat. Interdiscip. Top.* **1996**, *54*, 5377.
[33] G. P. Johari, M. Goldstein, *J. Chem. Phys.* **1970**, *53*, 2372.
[34] a) A. Kudlik, S. Benkhof, T. Blochowicz, C. Tschirwitz, E. Rössler, *J. Mol. Struct.* **1999**, *479*, 201; b) S. Kastner, M. Köhler, Y. Goncharov, P. Lunkenheimer, A. Loidl, *J. Non-Cryst. Solids* **2010**, *357*, 510.
[35] a) J. S. Harmon, M. D. Demetriou, W. L. Johnson, K. Samwer, *Phys. Rev. Lett.* **2007**, *99*, 135502; b) C. Gainaru, O. Lips, A. Troshagina, R. Kahlau, A. Brodin, F. Fujara, E. A. Rössler, *J. Chem. Phys.* **2008**, *128*, 174505; c) F. H. Stillinger, *Science* **1995**, *267*, 1935.
[36] J. Schnabel, A. Schulz, P. Lunkenheimer, D. Volkmer, *Commun. Chem.* **2023**, *6*, 161.
[37] S. Havriliak, S. Negami, *J. Polym. Sci.Polym. Symp.* **1966**, *14*, 99.
[38] A. K. Jonscher, *J. Phys. D: Appl. Phys.* **1999**, *32*, R57.
[39] a) S. R. Elliott, *Adv. Phys.* **1987**, *36*, 135; b) K. Funke, *Philos. Mag. A* **1993**, *68*, 711.
[40] a) R. Ameloot, M. Aubrey, B. M. Wiers, A. P. Gómora-Figueroa, S. N. Patel, N. P. Balsara, J. R. Long, *Chemistry* **2013**, *19*, 5533; b) J. Cepeda, S. Pérez-Yáñez, G. Beobide, O. Castillo, E. Goikolea, F. Aguesse, L. Garrido, A. Luque, P. A. Wright, *Chem. Mater.* **2016**, *28*, 2519; c) S. Niwa, M. Sadakiyo, *Dalton Trans. (Cambridge, England 2003)* **2022**, *51*, 12037.
[41] D. Reuter, C. Geiß, P. Lunkenheimer, A. Loidl, *J. Chem. Phys.* **2017**, *147*, 104502.
[42] a) M. D. Ediger, C. A. Angell, S. R. Nagel, *J. Phys. Chem.* **1996**, *100*, 13200; b) J. C. Dyre, *Rev. Mod. Phys.* **2006**, *78*, 953.
[43] F. Mizuno, J.-P. Belieres, N. Kuwata, A. Pradel, M. Ribes, C. A. Angell, *J. Non-Cryst. Solids* **2006**, *352*, 5147.
[44] T. Bauer, M. Köhler, P. Lunkenheimer, A. Loidl, C. A. Angell, *J. Chem. Phys.* **2010**, *133*, 144509.
[45] C. A. Angell, in *Relaxations in Complex Systems* (Eds. K. L. Ngai, G. B. Wright), Naval Research Laboratory, Washington, DC **1985**.
[46] a) P. G. Debenedetti, F. H. Stillinger, *Nature* **2001**, *410*, 259; b) J.-P. Bouchaud, G. Biroli, *Phys. Rev. B* **2005**, *72*, 064204.
[47] S. Albert, T. Bauer, M. Michl, G. Biroli, J.-P. Bouchaud, A. Loidl, P. Lunkenheimer, R. Tourbot, C. Wiertel-Gasquet, F. Ladieu, *Science* **2016**, *352*, 1308.
[48] G. Adam, J. H. Gibbs, *J. Chem. Phys.* **1965**, *43*, 139.
[49] a) F. Affouard, J.-F. Willart, M. Descamps, *J. Non-Cryst. Solids* **2002**, *9*; b) M. Michl, T. Bauer, P. Lunkenheimer, A. Loidl, *Phys. Rev. Lett.* **2015**, *114*, 67601; c) M. Pieruccini, E. Tombari, *Phys. Rev. E* **2018**, *97*, 32116.
[50] R. Böhmer, K. L. Ngai, C. A. Angell, D. J. Plazek, *J. Chem. Phys.* **1993**, *99*, 4201.
[51] N. Mardirossian, M. Head-Gordon, *J. Chem. Phys.* **2016**, *144*, 214110.
[52] J. Yu, S. Chang, X. Xu, X. He, C. Zhang, *J. Mater. Chem. C* **2020**, *8*, 8887.
[53] G. M. Sheldrick, *Acta Crystallogr., Sect. C: Struct. Chem.* **2015**, *71*, 3.
[54] T. D. Kühne, M. Iannuzzi, M. Del Ben, V. V. Rybkin, P. Seewald, F. Stein, T. Laino, R. Z. Khaliullin, O. Schütt, F. Schiffmann, D. Golze, J. Wilhelm, S. Chulkov, M. H. Bani-Hashemian, V. Weber, U. Borstnik, M. Taillefumier, A. S. Jakobovits, A. Lazzaro, H. Pabst, T. Müller, R. Schade, M. Guidon, S. Andermatt, N. Holmberg, G. K. Schenter, A. Hehn, A. Bussy, F. Belleflamme, G. Tabacchi, et al., *J. Chem. Phys.* **2020**, *152*, 194103.
[55] J. P. Perdew, K. Burke, M. Ernzerhof, *Phys. Rev. Lett.* **1996**, *77*, 3865.
[56] S. Grimme, J. Antony, S. Ehrlich, H. Krieg, *J. Chem. Phys.* **2010**, *132*, 154104.
[57] D. Dubbeldam, S. Calero, D. E. Ellis, R. Q. Snurr, *Mol. Simul.* **2016**, *42*, 81.
[58] A. K. Rappe, C. J. Casewit, K. S. Colwell, W. A. Goddard, W. M. Skiff, *J. Am. Chem. Soc.* **1992**, *114*, 10024.